Journal of
Materials Chemistry A

# Dual-phase modulation via Mo doping and Li3PO4 coating for stabilized LiNi0.9Mn0.07Co0.02Al0.01O2 cathodes in high-energy lithium-ion batteries

| | |
|---|---|
| Journal: | *Journal of Materials Chemistry A* |
| Manuscript ID | TA-ART-02-2025-001436.R1 |
| Article Type: | Paper |
| Date Submitted by the Author: | 26-Apr-2025 |
| Complete List of Authors: | Alagar, Srinivasan; Chungbuk National University, Deparment of Chemical Engineering<br>Park, Gi Dae; Chungbuk National University, Department of Advanced Materials Engineering<br>Kim, Jun; Chungbuk National University, Department of chemical engineering<br>Shin, Eun-Jung; Chungbuk National University, Department of Physics<br>Ditter, Alex; Lawrence Berkeley National Laboratory, Chemical Sciences Division<br>Shapiro, David; Lawrence Berkeley National Lab, Advanced Light Source<br>Kim, Namdong; Pohang Accelerator Laboratory<br>Hong, Won G.; Korea Basic Science Institute<br>Kim, Hyungsub; Korea Atomic Energy Research Institute, Neutron Science Center<br>Yu, Young-Sang; Chungbuk National University<br>Jeong, Sang Mun; Chungbuk National University, Department of Chemical Engineering |
| | |

Journal of Materials Chemistry A

PAPER

# Dual-phase modulation via Mo doping and $Li_3PO_4$ coating for stabilized $LiNi_{0.9}Mn_{0.07}Co_{0.02}Al_{0.01}O_2$ cathodes in high-energy lithium-ion batteries

Received 00th January 20xx,
Accepted 00th January 20xx

DOI: 10.1039/x0xx00000x

**www.rsc.org/**

Srinivasan Alagar,[a] Jun Kim,[a] Eun-Jung Shin,[b] Alex Ditter,[c] David A. Shapiro,[c] Namdong Kim,[d] Won Gi Hong,[eh] Hyungsub Kim,*[fh] Young-Sang Yu*[bh] Gi Dae Park*[gh] Sang Mun Jeong*[ah]

High-nickel layered oxide cathodes (Ni ≥ 90%) offer high capacity and energy density but face challenges like structural degradation and capacity fading during prolonged cycling. Herein, we report a novel Mo-doped $LiNi_{0.9}Mn_{0.07}Co_{0.02}Al_{0.01}O_2$ (Mo-NMCA) cathode coated with $Li_3PO_4$ (LPO) nanoscale coating, synthesized via an optimized co-precipitation and solid-state method for the first time. The Mo doping enhances structural stability by mitigating transition metal migration, while the LPO coating improves interfacial stability and ionic conductivity. The synergistic influence of doping and coating is specifically comprehended by neutron diffraction and scanning transmission X-ray microscopy analyses. Electrochemical analysis reveals that LPO-Mo-NMCA demonstrates an initial discharge capacity of 219 mA h $g^{-1}$ at 0.1 C and 176 mA h $g^{-1}$ at 1 C with a capacity retention of 87 % after 200 cycles. At a high C-rate of 3 C, the cathode retains 91 % of its initial capacity after 200 cycles, showcasing exceptional rate capability and cycling stability. Furthermore, we made a pouch-type full cells with LPO-Mo-NMCA and a graphite anode achieved an initial discharge capacity of 218 mA h $g^{-1}$ at 0.1 C, with 85 % capacity retention after 110 cycles. At a 3 C rate, these cells maintained 89 % capacity retention over 200 cycles in the voltage range of 2.0 to 4.2 V. These findings highlight LPO-Mo-NMCA as a promising cathode material for next-generation lithium-ion batteries, bridging the gap between high energy density and long-term cycling stability.

## 1. Introduction

High-nickel-content (≥90%) layered nickel-rich cathodes, specifically $Li[Ni_xCo_yMn_{1-x-y}]O_2$ (NCM) and $Li[Ni_xCo_yAl_{1-x-y}]O_2$ (NCA), have been widely utilized in electric vehicle batteries to address consumer concern over range anxiety.[1-4] While the layer cathodes have demonstrated remarkable capacity and cyclability even under high charging and discharging rates, nickel-rich cathodes often suffer from poor electrochemical performance and thermal stability, primarily due to intrinsic structural issues such as intergranular microcracks and side reactions.[5-7] The formation of microcracks, induced by uneven internal strain during the H2−H3 phase transition, undermines the mechanical integrity of the particles and facilitates electrolyte infiltration, which accelerates degradation.[5, 8, 9] To overcome these problems, synthetic strategies incorporating chemical engineering, such as elemental doping, surface coating, and morphology control, have been applied, leading to significant improvements in the cycling stability of Ni-rich cathodes.

Recent research has highlighted the promise of cathodes enhanced with high-valence-state dopants, such as Ta, Mo, W, B, Sb, and Nb, which are particularly effective in stabilizing the structure of Ni-rich cathodes by forming radially oriented and elongated primary particles within the secondary cathode particles.[10-13] The engineered morphologies effectively dissipate the uneven strain caused by lattice expansion or shrinkage between the charged and discharged chemical phases and minimize microcrack propagations even after prolonged cycling. Park et al. recently demonstrated that introducing Al, Mn, Ti, Ta, Sb, Nb, W, and Mo during the lithiation of Ni-rich hydroxide precursors yields morphologically well-engineered secondary cathode particles, characterized by elongated and interconnected primary particles with refined size and radial.[14] Additionally, the $Li^+/Ni^{2+}$ superlattice enhanced by the dopants acts as atomic pillars, supporting the Li−O layer and preventing collapse during deep delithiation.[15] The synergistic influences of high-valent dopants in Ni-rich cathodes (e.g., $LiNi_xMn_yCo_zM_{1-xyz}O_2$ with M being $Ta^{5+}$, $W^{6+}$, $Mo^{6+}$, etc.) enhance stability and energy density compared to traditional NCM90 and NCA90 cathodes.[16, 17] While the development of $LiNi_{0.9}Co_{0.09}M_{0.01}O_2$ cathodes with high-valent dopants offers an effective strategy for microstructure optimization,

[a]Department of Chemical Engineering, Chungbuk National University, Cheongju, Chungbuk 28644, Republic of Korea, E-mail: smjeong@chungbuk.ac.kr;
[b]Department of Physics, Chungbuk National University, 1 Chungdae-ro, Seowon-gu, Cheongju-si, Chungbuk-do 28644, Republic of Korea, E-mail: youngsang@chungbuk.ac.kr;
[c]Advanced Light Source, Lawrence Berkeley National Laboratory, Berkeley, CA 94720, USA
[d]Pohang Accelerator Laboratory, Pohang University of Science and Technology, Pohang 37673, Republic of Korea
[e]Research Center for Materials Ananlysis, Korea Basic Science Institute, Daejeon, Republic of Korea
[f]Neutron Science Division, Korea Atomic Energy Research Institute (KAERI),111 Daedeok-daero 989, Beon-Gil, Yuseong-gu, Daejeon 34057, Republic of Korea, E-mail: hyungsubkim@kaeri.re.kr;
[g]Department of Advanced Materials Engineering, Chungbuk National University, Chungdae-ro 1, Seowon-Gu, Cheongju, Chungbuk 28644, Republic of Korea, E-mail: gdpark@chungbuk.ac.kr;
[h]Advanced Energy Research Institute, Chungbuk National University, Chungdae-ro 1, Seowon-gu, Cheongju 28644, Republic of Korea

†Electronic Supplementary Information (ESI) available: [details of any supplementary information available should be included here]. See DOI: 10.1039/x0xx00000x
‡These authors contributed equally to this work.

the common reliance on solid-state synthesis methods often leads to inhomogeneous dopant distribution, resulting in improper dopant concentrations at the microscopic level.[18] Moreover, doping within the crystal structure intrinsically involves the substitution of active host ions with electrochemically inactive species, which can enhance ionic and electronic conductivity but often leads to poor electrochemical cycling performance and capacity decay.

A complementary approach to further enhancing the electrochemical performance of high-Ni NCM and related cathode materials is surface modification with an appropriate protective coating layer, applying at either the secondary or primary particle level,[5, 19] to mitigate side-reaction with electrolytes while simultaneously facilitating improved ionic/electronic diffusion and structural stability. [20, 21] Compared to doping, the coating strategy preserves the inherent characteristics of the cathode materials due to its strong localization on the surface. Among suitable coating materials, including metal oxides (e.g., $ZrO_2$, $Al_2O_3$, MgO, and ZnO), [22] fluorides, [23] phosphates, [24] carbon-based materials, [25] and fast lithium-ion conductors (e.g., $LiAlO_2$, $Li_{1.3}Al_{0.3}Ti_{1.7}(PO_4)_3$, $Li_2TiO_3$, $Li_2ZrO_3$, and $Li_3PO_4$,) demonstrate superior electrochemical performance compared to inert coatings such as oxides and fluorides. [26-28] The $Li_3PO_4$ (LPO) is favoured as a coating for Ni-rich cathodes because of its exceptional ionic conductivity (~$10^{-6}$ S $cm^{-1}$) [4, 26] and robust resistance to electrolyte-induced degradation. [29, 30]

Since innovative strategies to achieve uniform dopant distribution and stabilize the microstructure from bulk to surface are urgently demanded, particularly through a modified coprecipitation method that combines doping and coating processes, herein, a Mo-doped $LiNi_{0.9}Mn_{0.07}Co_{0.02}Al_{0.01}O_2$ (NMCA) cathode with a $Li_3PO_4$ (LPO) coating was fabricated using coprecipitation and solid-state methods for the first time. The optimized synthesis processes ensure a homogeneous Mo distribution, leading to a stable secondary microstructure with robustly bonded primary particles and a uniform LPO coating on the secondary particle surface. Mo preferentially migrates into the internal structure, enhancing cyclic stability, While LPO coating improves rate capability by stabilizing the surface structure, suppressing TM migration, and enhancing $Li^+$ transport, it does not significantly alter the bulk lattice spacing. Furthermore, the synergistic effect between the Mo-dopant and LPO coating significantly enhanced the electrochemical stability of the NMCA cathode compared to its pristine counterpart. This work offers a novel approach to substantially improve the electrochemical performance of Ni-rich cathodes for advanced lithium-ion batteries.

## 2. Experimental section

The spherical $Ni_{0.90}Mn_{0.07}Co_{0.02}Al_{0.01}(OH)_2$ precursor was synthesized via a well-established coprecipitation method using a 5 L batch reactor. Specifically, precise amounts of $NiSO_4 \cdot 6H_2O$, $MnSO_4 \cdot 6H_2O$, $CoSO_4 \cdot 7H_2O$, and $Al_2(SO_4)_3$ (in a molar ratio of Ni:Mn:Co:Al= 90 : 0.07 : 0.02 : 0.01) were dissolved in deionized water. This solution was continuously introduced into the reactor under a nitrogen atmosphere. Simultaneously, NaOH and $NH_4OH$ aqueous solutions were separately fed into the reactor. The synthesis was conducted at 60 °C, with the pH meticulously controlled at 11.5. Upon completion, the resulting precipitate was thoroughly washed with deionized water to remove residual impurities such as $Na^+$, $SO_4^{2-}$, and $NH_4^+$ ions. To synthesize $LiNi_{0.90}Mn_{0.07}Co_{0.02}Al_{0.01}O_2$, the precursor $Ni_{0.90}Mn_{0.07}Co_{0.02}Al_{0.01}(OH)_2$ powder was thoroughly mixed with $LiOH \cdot H_2O$ in a molar ratio of 1:1.05. The mixture was then calcined at 750 °C for 12 hours under an oxygen atmosphere (heating rate 2 °C $min^{-1}$. The resulting cathode material was designated as $LiNi_{0.90}Mn_{0.07}Co_{0.02}Al_{0.01}O_2$ (NMCA). For the preparation of Mo-doped $LiNi_{0.90}Mn_{0.07}Co_{0.02}Al_{0.01}O_2$ (Mo-NMCA) materials, ammonium molybdate $(NH_4)_6Mo_7O_{24}$ was dissolved in ethanol under continuous stirring (designated as solution A) at doping levels of 0.2, 0.3, and 0.4 mol%. Meanwhile, the wet $Ni_{0.90}Mn_{0.07}Co_{0.02}Al_{0.01}(OH)_2$ precursor was dispersed in ethanol with stirring (designated as solution B). Solution A was gradually added to solution B under vigorous stirring at room temperature. After 5 hours of stirring, the mixture was heated to 60 °C to evaporate the solvent while maintaining constant agitation. The Mo-doped NMCA was then mixed with $LiOH \cdot H_2O$ using 3D mixing for 2 hours, followed by calcination at 550 °C for 5 hours and 750 °C for 12 hours in an oxygen-rich atmosphere. The resulting Mo-doped $LiNi_{0.90}Mn_{0.07}Co_{0.02}Al_{0.01}O_2$ (Mo-NMCA) was obtained with Mo doping levels of 0.2, 0.3, and 0.4 mol%, denoted as Mo2-NMCA, Mo-NMCA, and Mo4-NMCA, respectively.

To further optimize the material, Mo-NMCA with 0.3 mol% Mo (Mo3-NMCA) was coated with $Li_3PO_4$ (LPO). Initially, $LiNO_3$ and $H_3PO_4$ were dissolved in ethanol under stirring to form solution A. Concurrently, the optimized Mo3-NMCA was dispersed in ethanol under stirring to form solution B. Solution A was added dropwise to solution B with rapid stirring at room temperature. After 5 hours of stirring, the mixture was heated to 80 °C to evaporate the solvent while continuing to stir. The $Li_3PO_4$ content was adjusted to 1, 2, and 4 wt%, hereafter referred to as LPO1-Mo-NMCA, LPO2-Mo-NMCA (LPO-Mo-NMCA), and LPO4-Mo-NMCA, respectively, by varying the amounts of $LiNO_3$ and $H_3PO_4$. The LPO coated cathodes were then sintered at 500 °C for 3 hours in an oxygen atmosphere.

## 3. Results and Discussion

In this study, a co-precipitation technique was innovatively designed to synthesize spherical $Ni_{0.90}Mn_{0.07}Co_{0.02}Al_{0.01}(OH)_2$ precursors, as validated by X-ray Diffraction (XRD) and Field Emission Scanning Electron Microscopy (FE-SEM) images, as detailed in Supporting Information (Fig. S1-S2). The crystal structures of the NMCA, Mo-NMCA, and LPO-Mo-NMCA samples were characterized using XRD and Neutron Diffraction (ND) analyses. Fig. 1a presents the XRD patterns of the samples, which align with the hexagonal α-$NaFeO_2$ structure (space group *R-3m*, JCPDS *No.* 09-0063). The distinct splitting of the (006)/(012) and (018)/(110) reflections confirms that the well-ordered layered structure was preserved after doping and coating. [11] A trace amount of residual lithium compound ($Li_2CO_3$) was detected in all samples, along with weak LPO signals in the LPO-Mo-NMCA pattern within 21–25°. To obtain detailed atomic-level information, ND analyses were conducted, as shown in Fig. 1b-d. The lattice parameters derived from Rietveld refinement, summarized in Table S1. The Mo incorporation, the lattice parameters exhibited a clear expansion, with the a-axis increasing from 2.87754 to 2.88070 Å, the c-axis from 14.1997 to 14.2164 Å, and the unit cell volume from 101.824 to 102.169 Å³. This expansion is attributed to the substitutional introduction of $Mo^{6+}$ into the

 

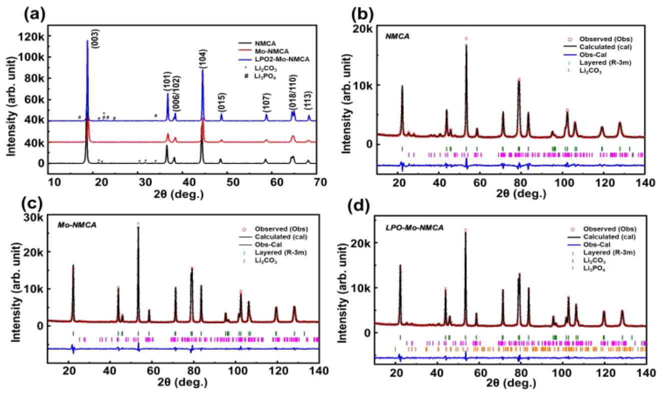


**Fig. 1** (a) Powder XRD patterns of NMCA, Mo-NMCA, and LPO-Mo-NMCA samples. ND analyses of (b) NMCA, (c) Mo- NMCA, and (d) LPO-Mo- NMCA cathodes.

transition metal layer, resulting in local lattice distortion and interlayer expansion, which are favourable for accelerated $Li^+$ diffusion. Conversely, the application of $Li_3PO_4$ coating led to a mild lattice contraction (a = 2.87288 Å, c = 14.1950 Å, volume = 101.462 Å³), indicating that the surface treatment preserved the bulk structural integrity while enhancing surface passivation. Furthermore, site occupancy analysis revealed that the extent of $Ni^{2+}$ occupancy in the Li layer (indicating cation disorder) increased with Mo doping (0.088) compared to pristine NMCA (0.038), whereas it was significantly suppressed in the LPO-Mo-NMCA sample (0.021), demonstrating the effectiveness of the $Li_3PO_4$ coating in mitigating Li/Ni cation disorder. Moreover, $Ni^{2+}$ occupancy in the Li layer increased from 3.8% (NMCA) to 8.8% (Mo-NMCA), but decreased to 2.1% in LPO-Mo-NMCA, supported by improved $R_{wp}$ (5.30% to 3.83%) and $R_F$ (1.33% to 1.04%). While LPO cannot reverse initial cation mixing, it effectively limits further disorder, enhancing the structural stability of the cathode. These structural evolutions collectively illustrate the dual function of Mo doping and LPO surface engineering in tuning the lattice architecture and stabilizing the layered framework, which synergistically contribute to enhanced $Li^+$ transport kinetics and structural robustness during electrochemical cycling.[31] Additional XRD patterns for the Mo1-NMCA, Mo3-NMCA, Mo4-NMCA, LPO1-Mo-NMCA, and LPO4-Mo-NMCA cathode materials are provided in Fig. S3, further corroborating the phase purity and uniformity of the synthesized materials. Collectively, these findings emphasize the success of the structural and morphological design, which supports the robustness and electrochemical viability of the developed cathode materials.

Field-emission scanning electron microscopy (FE-SEM) and transmission electron microscopy (TEM) were employed to analyse the structural characteristics of the NMCA, Mo-NMCA, and LPO-Mo-NMCA samples, as depicted in Fig. 2 and 3. The FE-SEM images of NMCA (Fig. 2a and b), Mo-NMCA (Fig. 2c,d), and LPO-Mo-NMCA (Fig. 2e and f) demonstrate that all samples exhibit a well-defined spherical morphology, with secondary particle sizes uniformly distributed within the 2–3 µm range. At 60 KX magnification (Fig. 2 c, f and i), the NMCA sample (Fig. 2c) reveals loosely agglomerated primary particles with relatively smooth and well-faceted surfaces, which suggest minimal surface disorder and weak interparticle fusion. In contrast, the Mo-NMCA (Fig. 2f) and LPO-Mo-NMCA (Fig. 2i) samples exhibit more densely packed and structurally fused

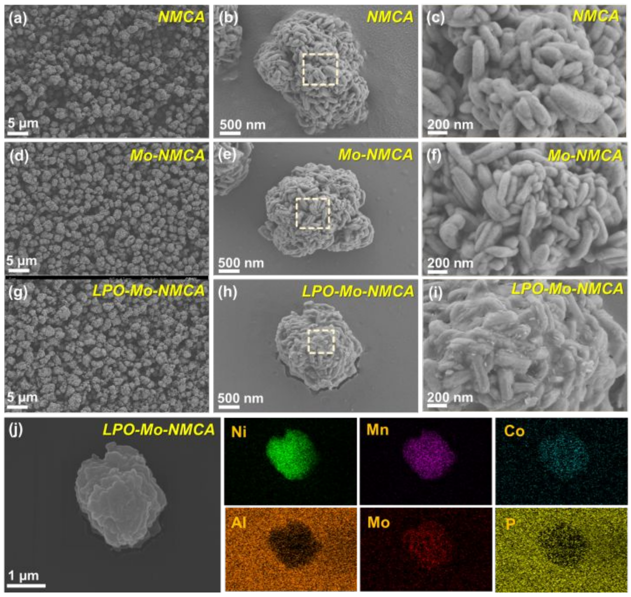


**Fig. 2** FE-SEM images showcasing the morphology of (a-c) NMCA, (d-f) Mo-NMCA, and (g-i) LPO-Mo-NMCA at low (e,h) and high (f,i) magnifications. (j) FE-SEM image of LPO-Mo-NMCA, accompanied by elemental mapping of Ni, Mn, Co, Al, P, and Mo, illustrating their spatial distributions.

primary grains, indicating enhanced interparticle connectivity and compactness a morphological evolution likely facilitated by Mo doping and subsequent LPO surface modification.

Following the LPO modification, the presence of uniform coating layer is observed on the Mo-NMCA surface, as evidenced by the inset FE-SEM image (Fig. 2f) and energy-dispersive X-ray spectroscopy (EDS) spectra mapping (Fig. 2g) further validate the homogeneous distribution of phosphorus across the particle surface, thereby affirming the spatial uniformity of the LPO layer. This coating not only contributes to the uniformity of the particle surfaces but also potentially enhances the structural stability of the material by providing additional protection against surface degradation. Further analysis, as depicted in Fig. S4-S6, includes EDS spectra and mapping to examine the elemental distribution within NMCA and Mo-NMCA samples. The results clearly demonstrate the presence of the LPO layer on the Mo-NMCA surface, with P atoms uniformly distributed across the surfaces of the secondary particles. This even distribution is indicative of the successful coating of LPO, which may play a critical role in enhancing electrochemical performance and overall stability.

TEM was employed to analyze the morphology and elemental distribution of pristine NMCA (Fig. S6) and LPO-Mo-NMCA (Fig. 3g), with particular attention to identifying the LPO surface layer. The primary particles exhibit well-defined faceted shapes, with average sizes of ~290 nm for NMCA (Fig. S6a) and ~162 nm for LPO-Mo-NMCA (Fig. S7a), as confirmed by EDX elemental mapping (Figs. S6b–f and 3g). The HR-TEM image of the pristine NMCA cathode reveals radially oriented, elongated grains across the primary particle (Fig. 3a). The [003] zone axis analysis indicates a typical layered structure and an ordered superlattice, as confirmed by the FFT patterns in Fig. 3a and e. In contrast, the LPO-Mo-NMCA cathode preserves a similar morphology and crystal structure, as seen in the HR-TEM images of the primary particle (Fig. 3d). A slight increase in the (003) plane spacing is noted, from 0.477 nm in pristine NMCA to 0.478 nm in

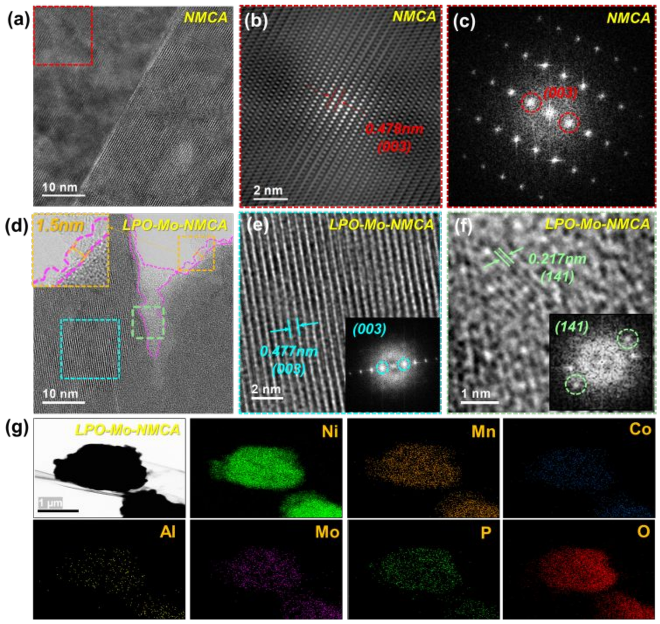


**Fig. 3** HR-TEM images of (a) pristine NMCA with (b) corresponding FFT pattern and (c) indexed hkl planes. (d) HR-TEM image of LPO-Mo–NMCA and (e, f) associated FFT patterns (inset: (hkl) planes). (g) TEM image of LPO–Mo–NMCA with EDX mapping showing uniform distribution of Ni, Mn, Co, Al, Mo, P, and O.

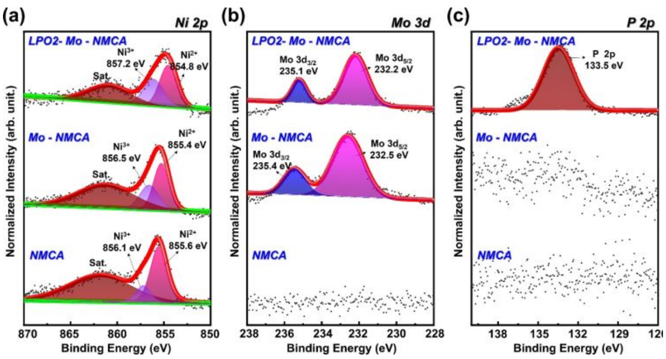


**Fig. 4** XPS spectra of NMCA, Mo-NMCA and LPO-Mo-NMCA samples: (a) Ni 2p, (b) Mo 3d and (c) P 2p.

LPO-Mo-NMCA, observed in Fig. 3b and e, suggesting that the LPO coating induces minor structural changes. The LPO coating is clearly visible as a 1.5 nm thick amorphous layer, which is confirmed through HR-TEM imaging and FFT patterns (Fig. 3d). Additionally, the interplanar spacing of 0.217 nm corresponds to the (141) plane, further supporting the identification of the coating as LPO, as shown in Fig. 2f. The slight reduction in d-spacing for the coated sample is attributed to interfacial compressive stress generated during post-coating annealing, arising from the mismatch in thermal expansion coefficients between the LPO shell and pristine NMCA.[31, 32] These modifications, through doping and coating, significantly enhance the performance and durability of lithium-ion batteries. Doping reinforces the crystal lattice, improves capacity retention, and mitigates issues such as transition metal migration, while coating with LPO acts as a protective layer that reduces side reactions, enhances interfacial stability, and preserves surface integrity. Collectively, these enhancements contribute to improved structural stability, more uniform ion distribution, and extended battery lifespan.

X-ray photoelectron spectroscopy (XPS) was employed to characterize the oxidation states of key elements. As shown in Fig. 4a, the Ni 2p spectra for NMCA, Mo-NMCA, and LPO-Mo-NMCA cathodes reveal a shift in the primary Ni $2p_{3/2}$ peak from 855.64 eV in NMCA to 854.84 eV in LPO-Mo-NMCA, reflecting a lower binding energy. This shift suggests a higher $Ni^{3+}$ concentration, confirming the coexistence of $Ni^{2+}$ and $Ni^{3+}$ oxidation states within LPO-Mo-NMCA, consistent with previous studies. [33] Elevated levels of $Ni^{2+}$ are typically associated with greater cation disorder, due to the comparable ionic radii of $Li^{+}$ and $Ni^{2+}$ and the lower energy requirements for Li/Ni exchange. [34] Consequently, the LPO-Mo-NMCA sample demonstrates reduced $Li^{+}/Ni^{2+}$ intermixing, enhancing structural stability. Furthermore, a satellite peak at 861.23 eV in the XPS spectra confirms the divalent Ni state. Additionally, we performed argon ion sputtering XPS depth profiling to examine the $Ni^{2+}$ and $Ni^{3+}$ states at different depths, up to 70 nm. While direct deconvolution of $Ni^{3+}$ peaks is challenging due to spectral overlap, we observed clear shifts in the Ni $2p_{3}/_{2}$ binding energy. This shift toward lower energies with increasing depth suggests a decrease in $Ni^{2+}$ content and more stable Ni oxidation states. We have now included the $Ni^{3+}/Ni^{2+}$ ratio trend (Fig. S8), which shows an increase in $Ni^{3+}$ from 64.85% at the surface to 81.12% at 50 nm depth profile. Regarding the role of the LPO surface coating, although it is applied post-synthesis, the subsequent annealing at 500 °C induces a strong chemical interaction between the LPO layer and the cathode surface. This thermal treatment not only suppresses surface oxygen loss but also stabilizes Ni in a higher oxidation state, thereby minimizing the formation of $Ni^{2+}$ and mitigating Li/Ni disorder. Moreover, the LPO coating acts as a surface passivation layer, reducing side reactions and improving structural and electrochemical stability. In Fig. 4b, Mo incorporation is further substantiated by deconvoluted peaks at Mo $3d_{5/2}$ and Mo $3d_{3/2}$, observed in both Mo-NMCA and LPO-Mo-NMCA, with Mo 3d binding energies aligning closely with established literature values, verifying the successful integration of Mo into the structure.[3] Finally, Fig. 4c shows a distinct P 2p peak in the LPO-Mo-NMCA, confirming phosphorus incorporation. This P 2p peak is resolved into P $2p_{3/2}$ and P $2p_{1/2}$ components, attributed to phosphate species (e.g., $PO_4^{3-}$). [31, 35]

Fig. 5a presents the galvanostatic charge/discharge profiles for NMCA, Mo-NMCA, and LPO-Mo-NMCA samples tested at 0.1 C (1 C = 220 mA h $g^{-1}$) within the potential range of 2.8–4.3 V. The initial specific discharge capacities for NMCA, Mo2-NMCA, Mo-NMCA, Mo4-NMCA, LPO1-Mo-NMCA, LPO-Mo-NMCA, and LPO4-Mo-NMCA were 179, 184, 196, 132, 161, 219, and 165 mA h $g^{-1}$, with corresponding initial coulombic efficiencies of 89, 88, 75, 81, 92, and 90 %, respectively. The increased discharge capacity and coulombic efficiency in Mo-doped and LPO-coated NMCA materials can be attributed to several factors. Mo doping in the Ni sites likely enhances structural stability and reduces transition metal migration, leading to better overall electrochemical performance. This doping also improves electronic conductivity and facilitates more efficient $Li^{+}$ ion diffusion, contributing to higher discharge capacities. Additionally, the LPO coating on the Mo-NMCA surface acts as a protective barrier, minimizing side reactions at the electrode-electrolyte interface and preserving the active materials integrity during cycling. The LPO layer also enhances interfacial stability, improving $Li^+$ ion intercalation/deintercalation processes, which results in superior coulombic efficiency and discharge capacity. Collectively, the synergistic effects of Mo doping and LPO coating significantly optimize the electrochemical properties of NMCA, leading to enhanced performance. Fig. 5b further illustrates the initial three charge/discharge cycles of LPO-Mo-NMCA, revealing a superior profile, with the 2nd and 3rd cycles exhibiting a discharge capacity of 216 mA h $g^{-1}$ and a coulombic efficiency of 98.7 %. The dQ/dV profile in Fig. 5c delineates a sequential phase transition (H1–M–H3) that unfolds progressively during charging and discharging. Notably, across cycles 2, 10, 20, 30, 40, and 50, the robust alignment of the H2–H3 peak in LPO-Mo-NMCA demonstrates sustained structural integrity and reversible capacity retention, affirming its enhanced structural stability and electrochemical reversibility over prolonged cycles. Fig. 5d shows the extended cycling behavior over 50 cycles, indicating a high-capacity retention of 85 %.

The high-rate capability of the NMCA, Mo-NMCA and LPO-Mo-NMCA (Fig. 5e) cathode demonstrates impressive discharge performance across various C-rates, ranging from 0.2 to 5 C. At a 0.2 C rate, the cathode exhibits a reversible capacity of 150.7, 170.4 and 208.7 mA h $g^{-1}$ for NMCA, Mo-NMCA and LPO-Mo-NMCA cathodes respectively. Even at an elevated 5 C rate 31.5 (47.6 mA h $g^{-1}$), 51.4 % (87.6 mA h $g^{-1}$) and 74.5 % (155.5 mA h $g^{-1}$) it retains of capacity. Remarkably, when the rate is reset to 0.2 C, the capacity is nearly fully restored to 197 mA h $g^{-1}$, surpassing that of LPO-Mo-NMCA cathodes. This retention and recovery highlight the superior structural resilience of LPO-Mo-NMCA, underscoring its suitability comparison among NMCA, Mo-NMCA, and LPO-Mo-NMCA cathodes reveals consistently superior performance of LPO-Mo-NMCA. As shown in Fig. 5f, the electrochemical long-term cycling performance for high-rate and long-term cycling application. The cyclic stability highlights the superior stability of LPO-Mo-NMCA compared to NMCA and Mo-NMCA under both moderate and high-rate

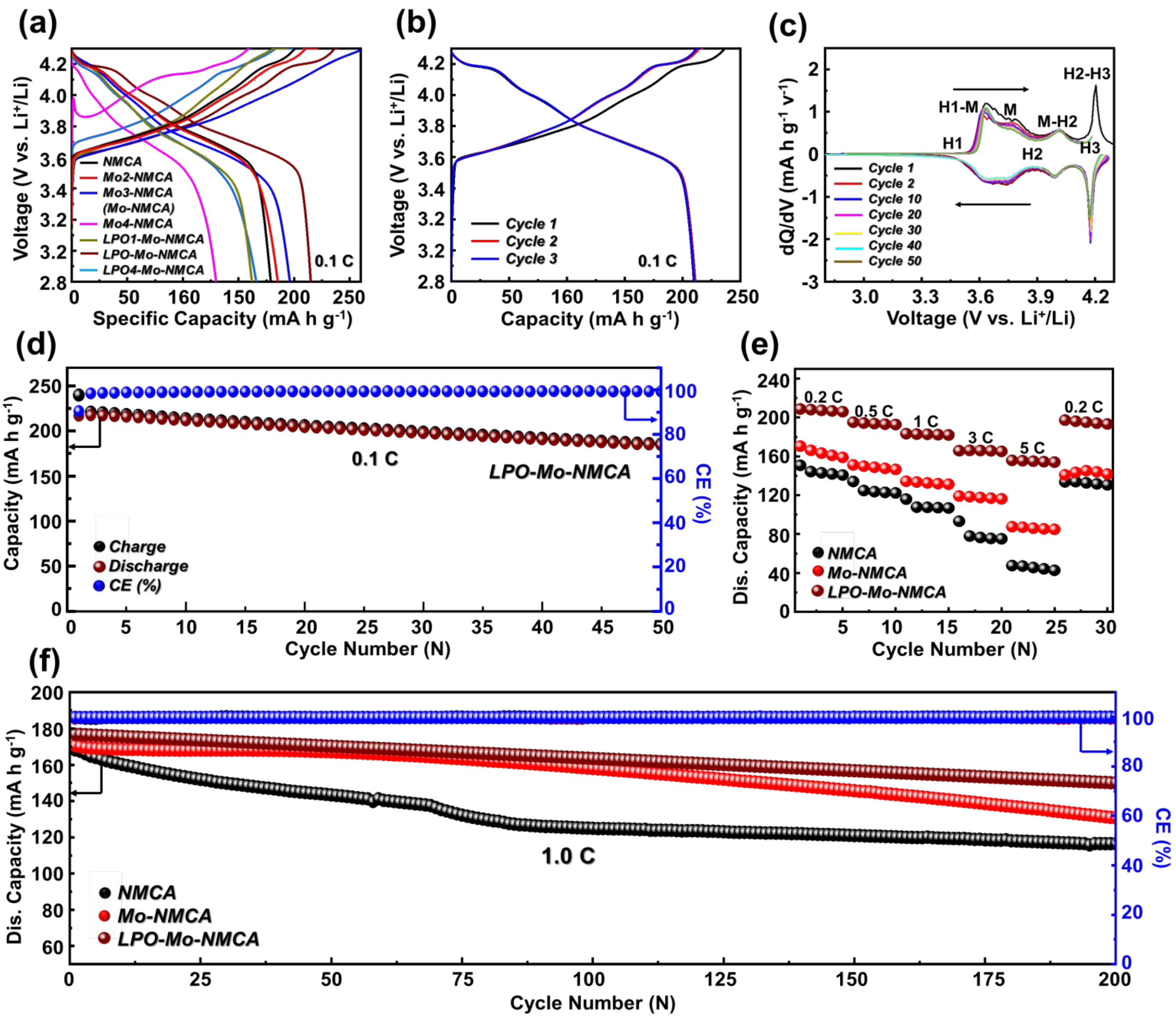


**Fig. 5** (a) Initial charge-discharge curves at 0.1 C, (b) the initial three cycles of LPO-Mo-NMCA at 0.1 C, (c) dQ/dV profiles for the first three cycles (d) cycling performance of LPO-Mo-NMC for 50 cycles at 0.1 C, (e) rate capabilities, and (f) long-term cycling performances of NMCA, Mo-NMCA, and LPO-Mo-NMCA at 1 C for 200 cycles.

 

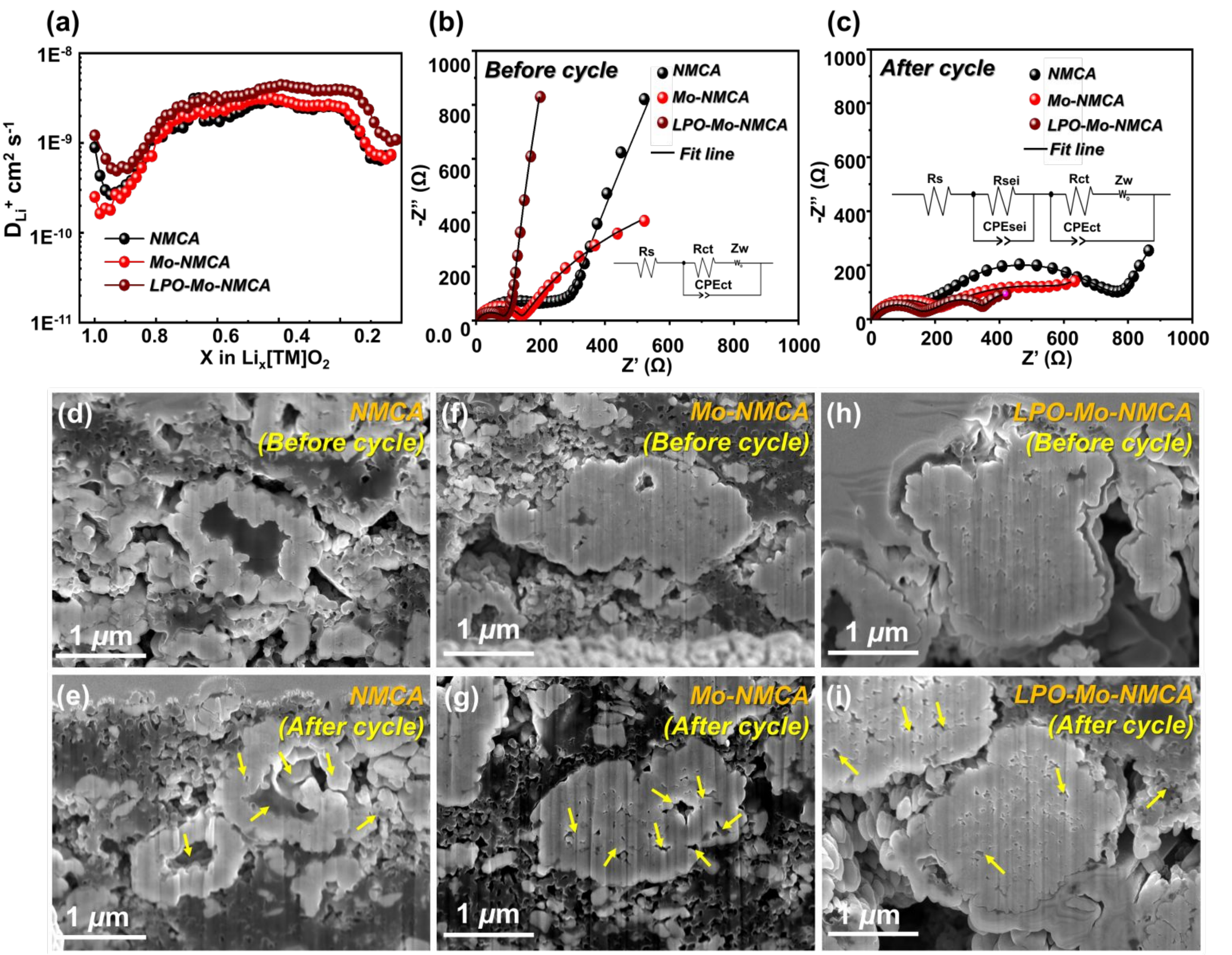


**Fig. 6** (a) Li-ion diffusion coefficients estimated from the GITT data, EIS spectra of (b) before and (c) After 200 cycle at 1 C. Cross-sectional SEM images of particles from electrodes before and after 200 charge/discharge cycles at 1 C reveal significant morphological distinctions between (d, e ) NMCA and (f, g) Mo-NMCA and (h, i) LPO-Mo-NMCA samples.

conditions. At a 1 C rate, the initial discharge capacities for NMCA, Mo-NMCA, and LPO-Mo-NMCA are 168, 170, and 176 mA h $g^{-1}$, respectively, with NMCA and Mo-NMCA retaining only 69 and 76% of their capacities after 200 cycles. In contrast, the LPO-Mo-NMCA cathode exhibits remarkable durability, retaining 87 % of its initial capacity. At a more demanding 3 C rate (Fig. S9), the initial discharge capacities are 123, 137, and 128 mA h $g^{-1}$ for NMCA, Mo-NMCA, and LPO-Mo-NMCA, respectively. Over 200 cycles, NMCA and Mo-NMCA demonstrate significant capacity fading, retaining only 49 and 56% of their original values, respectively, while LPO-Mo-NMCA sustains 91 % of its capacity. This enhanced stability underscores the synergistic influence of Mo doping and LPO surface modification in fortifying the cathode architecture, mitigating structural degradation, and significantly advancing long-term electrochemical resilience under high-rate cycling conditions. These results validate Mo and LPO modifications as effective approaches to extending the operational lifespan and reliability of high-energy cathode materials for demanding applications.

To comprehensively understand the impact of LPO coating and Mo doping on lithium-ion diffusion during the charging process, the galvanostatic intermittent titration technique (GITT) was utilized, as shown in Fig. S10 a–c. The GITT profiles for NMCA, Mo-NMCA, and LPO-Mo-NMCA cathodes demonstrate comparable trends in $D_{Li}^+$ values, with slight deviations observed under deeply charged conditions (Fig. 6a). Across all samples, the diffusion coefficient exhibits a gradual increase, stabilizing at a plateau around x = 0.4. Remarkably, the LPO-Mo-NMCA cathode showcases enhanced $D_{Li}^+$ values compared to its NMCA and Mo-NMCA counterparts, attributed to the combined benefits of Mo doping and LPO surface modifications. In contrast, NMCA and Mo-NMCA cathodes exhibit comparatively reduced diffusion coefficients, aligning with anticipated trends. As depicted in Fig. 6a, $D_{Li}^+$ values during the early stages of charging are in the range of ~$10^{-11}$ $cm^2$ $s^{-1}$, subsequently rising to $10^{-10}$ – $10^{-9}$ $cm^2$ $s^{-1}$ at later stages.[36] These findings indicate that the introduction of Mo and LPO modifications significantly enhances lithium-ion transport properties by mitigating migration barriers and stabilizing the layered structure. The $Li^+$ diffusion coefficients obtained values are compared with the previously reported values in the literature, as presented in Table S2. The electrochemical performance of NMCA cathode materials was systematically investigated to unravel the effects of Mo doping and LPO surface coating, with electrochemical impedance spectroscopy

(EIS) serving as the principal analytical technique. As shown in Fig. 6b,c, Nyquist plots of the pristine and after 200 cycles at 1 C. Initially, the spectra exhibit a single depressed semicircle in the high-to-medium frequency region, followed by an inclined line in the low-frequency region, which corresponds to charge-transfer resistance ($R_{ct}$) and Li-ion diffusion, respectively. After prolonged cycling, the spectra evolve to show two well defined semicircles at high and medium frequencies associated with the solid electrolyte interphase resistance ($R_{SEI}$) and $R_{ct}$, along with a Warburg diffusion tail. To quantitatively analyze the interfacial characteristics and kinetic behavior, we fitted the EIS spectra using an equivalent circuit model (insets in Fig. 6b,c) consisting of solution resistance ($R_s$), $R_{SEI,}$ $R_{ct}$, and Warburg impedance (W). As summarized in Table S3, before cycling, the pristine NMCA electrode exhibited a high $R_{ct}$ of 248.54 Ω and a diffusion coefficient ($D_{Li^+}$) of 8.17 × $10^{-12}$ $cm^2{\cdot}s^{-1}$. In contrast, Mo doping significantly reduced $R_{ct}$ to 141.54 Ω, with improved $D_{Li^+}$ of 2.32 × $10^{-12}$ $cm^2{\cdot}s^{-1}$. LPO surface coating further suppressed $R_{ct}$ to 89.85 Ω and boosted $D_{Li^+}$ to 2.05 × $10^{-11}$ $cm^2{\cdot}s^{-1}$, confirming enhanced charge-transfer kinetics and bulk diffusion. After 200 cycles, NMCA showed a drastic increase in total interfacial resistance ($R_{SEI}$ + $R_{ct}$ = 890.58 Ω), along with a sharp drop in $D_{Li^+}$ to 4.29 × $10^{-13}$ $cm^2{\cdot}s^{-1}$, indicating severe impedance buildup and sluggish kinetics. In comparison, Mo-NMCA retained a lower combined resistance (771.2 Ω) and a higher $D_{Li^+}$ of 8.32 × $10^{-13}$ $cm^2{\cdot}s^{-1}$. Remarkably, LPO-Mo-NMCA maintained the lowest $R_{SEI}$ + $R_{ct}$ value (404.13 Ω) and a superior $D_{Li^+}$ of 1.46 × $10^{-12}$ $cm^2{\cdot}s^{-1}$, signifying a stable and conductive CEI layer. Remarkably, the coated samples exhibited significantly lower charge-transfer resistance (*$R_{ct}$*), reflecting enhanced $Li^+$ ion transport kinetics and diminished polarization effects. Furthermore, the Mo and LPO-coated NMCA electrodes demonstrated the formation of a thinner and more stable SEI layer compared to pristine NMCA and Mo-doped NMCA, translating into superior cycling stability and extended electrode lifespan.

To assess the degree of microcrack formation due to cycling, post-cycled secondary particles from electrodes were precisely sectioned using focused ion beam (FIB) technology, enabling SEM-based cross-sectional examination (Fig. 6d-i). Significant microcracks were detected along the grain boundaries of primary particles in both NMCA (Fig. 6 d and e**)** and Mo-NMCA (Fig. 6f and g), where continued cycling exacerbated the detachment between these particles, leading to severe structural degradation. In contrast, the LPO-Mo-NMCA cathode particle retained an exceptionally intact primary particle arrangement, with minimal microcrack presence as shown in Fig. 6 h and i. This structural integrity suggests that the LPO-Mo coating effectively alleviates interparticle strain, thereby preventing microcrack propagation and enhancing overall cycling stability. These findings underscore the LPO-Mo coating's role as a critical factor in improving the long-term durability of cathode materials under high-stress cycling conditions.

XPS analysis reveals significant advancements in Ni-rich cathodes achieved through Mo doping and $Li_3PO_4$ surface coating. This dual strategy effectively reduced residual lithium impurities, with $Li_2CO_3$ levels decreasing from 15.98 % in NMCA to 13.44 % in Mo-NMCA and 8.77 % in LPO-Mo-NMCA, as demonstrated in storage tests at 25 °C, over the $1^{st}$ and $200^{th}$ cycles (Fig. 7 a and b). The $Li_3PO_4$ coating formed a robust and chemically stable passivation layer, suppressing oxygen loss by limiting interactions with air and

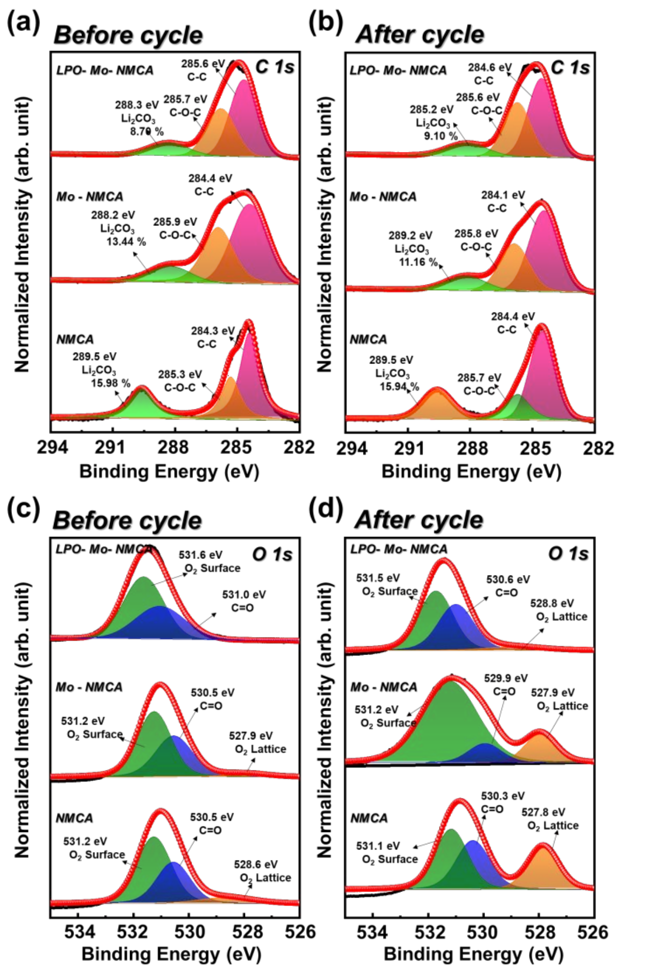


**Fig. 7** XPS spectra of (a) before and (b) after cycle of C 1s spectra and (c) before and after of O 1s spectra of NMCA, Mo-NMCA, and LPO-Mo-NMCA cathode samples.

moisture, while also mitigating surface degradation processes. $Mo^{6+}$ incorporation into the NMCA the lattice-oxygen signal in the O 1s spectrum shifts to higher binding energy, reflecting increased positive polarization of the oxygen anions by high-valence $Mo^{6+}$ and therefore stronger M–O bonds. Concurrently, the defect-related component diminishes in intensity, indicating a reduction in oxygen vacancies. These two spectral changes binding energy increase and defect-O2 lattice decrease, demonstrate that $Mo^{6+}$ stabilizes the $O_2$- lattice and inhibits cation disorder,[37, 38] as evidenced by O1s XPS spectra (Fig. 7 c and d). The combined effects of surface passivation and lattice stabilization resulted in enhanced chemical and structural integrity, improved cycling stability, and suppressed degradation mechanisms. This approach offers a promising pathway for achieving high-performance and durable Ni-rich cathode materials.

The strong correlations between structural integrity and electrochemical degradation were further highlighted through morphologically and shown in Fig. 8 and 9. Detailed information on the STXM analysis is provided in the Supplementary Materials. At the secondary particle level, the synergistic effect of Mo-dopant and LPO coating appears to promote densely packed primary particles (Fig. 8a and d) and and e). The averaged $i^{2+}$ compositions across the entire sample region are 25.6 % for pristine LPO-Mo-NMCA and 64.8 % for pristine NMCA, respectively (Fig. 8c and f). Furthermore, quantitative

 

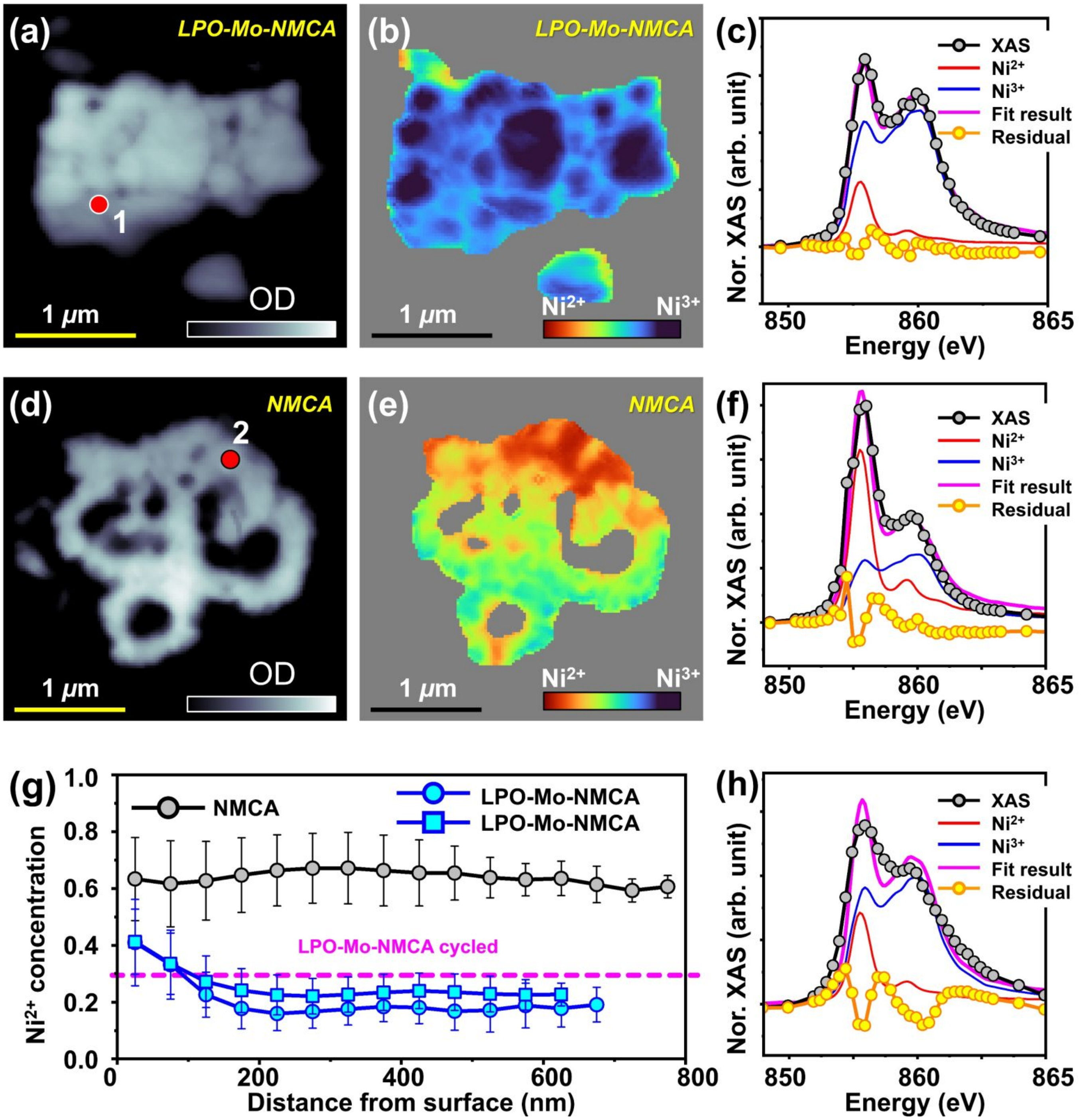


**Fig. 8** Microstructures and Ni oxidation state distribution maps of X-ray-transparent FIB-sliced (a, b) LPO-Mo-NMCA, (d and e) NMCA, with corresponding averaged XAS spectra (c and b) obtained from the entire sample region using STXM (g) Dependence of the average Ni oxidation state on the distance from the surface of the secondary particle for LPO-Mo-NMCA (blue line with square scatter) and NMCA (black line with circle scatter) as shown in (a) and (d), respectively. Additional STXM analysis results, shown in Fig. S13, are also plotted as a blue line with circle scatter. The Ni2+ composition obtained from the averaged XAS spectrum for 200 cycled LPO-Mo-NMCA in (h) is marked with a magenta dotted line for comparison. Microstructural information (a and d) was estimated from the mean optical densities across the Ni L-absorption edge. Pixel-by-pixel XAS spectra in the chemical maps (b and e) and the averaged XAS spectra (c, f, and h) were quantitatively

Ni oxidation state mapping conducted *via* STXM reveals that the $Ni^{2+}$ concentration in pristine LPO-Mo-NMCA secondary particles is highest at the surface, rapidly decreasing within a 200 nm range in the near-surface region and remaining nearly constant towards the center. Since the particles were randomly selected, the $Ni^{2+}$ compositional values may differ from the overall Ni oxidation state in the full cathode, making it challenging to represent the exact degree of degradation for each sample. However, bulk analyses (Fig. 1 and 4) demonstrate a similar trend regarding the presence of dopants and coatings, supporting the representativeness of our STXM measurements Additionally, the similar trend observed for an independent particle, as shown in Fig. S13, further supports the

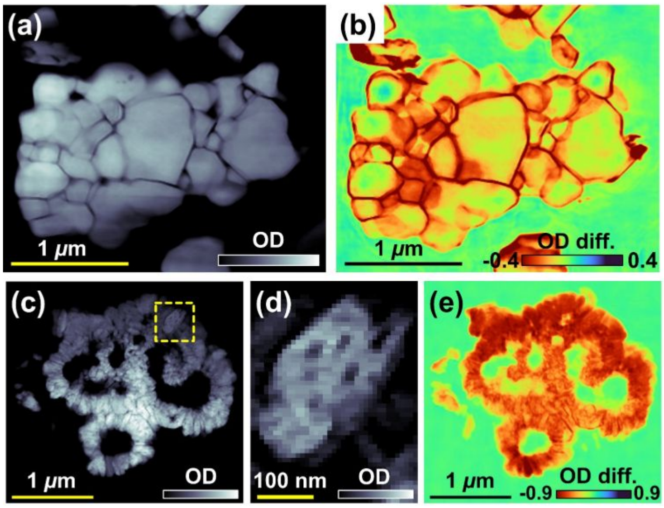


**Fig. 9** Optical density and qualitative chemical maps of X-ray-transparent FIB-sliced pristine LPO-Mo-NMCA (a and b) and NMCA (a, d and e) obtained using high-resolution ptychography. (d) Zoomed-in optical density map corresponding to the yellow dotted box marked in (c). The optical density maps (a, c, and d) were measured at 855.1 eV. Qualitative chemical information was acquired from the optical density difference between 852.7 and 855.1 eV. The optical density maps at 852.7 eV are shown in Fig. S15. The reddish color in the qualitative chemical maps (b and e) indicates a relatively higher concentration of $Ni^{2+}$.

reproducibility of our findings and underscores the reliability of the STXM-based $Ni^{2+}$ distribution analysis. To ensure the representativeness of the selected secondary particle, additional STXM analysis was conducted on a different pristine LPO-Mo-NMCA secondary particle, yielding an almost identical trend in the distribution of $Ni^{2+}$, as shown in Fig. S13. In contrast, the $Ni^{2+}$ concentration in bare NMCA is higher overall and shows no dependency on proximity to the external surface. Note that the accuracy of the pixel-by-pixel quantitative $Ni^{2+}$ composition obtained via linear superposition of the reference spectra was clearly validated by the single-pixel spectral analysis results shown in Fig. S12. The two possible origins of the observed gradient in $Ni^{2+}$ are: (1) oxygen vacancies in the near-surface volume of the secondary particles, leading to a composition resembling $LiMO_{2-\delta}$ due to high temperature and prolonged treatments [39] and (2) the formation of a disordered rock-salt structure, represented as $Li_{1-x}M_{1+x}O_2$ during the synthesis process [40]. Notably, even with a significant proportion of $Ni^{2+}$ present either within the 200-nm surface region of LPO-Mo-NMCA or throughout the entire region of NMCA, all synthesized cathodes maintain a well-defined layered structure without detectable rock-salt impurity phases in their pristine state, as evidenced by the XRD results shown in Fig. 1. The internal surfaces resulting from the hollow structure in NMCA may cause the entire volume to behave like near-surface volume during the synthesis procedure, accelerating oxygen vacancy creation throughout the sample and ultimately leading to a significantly higher overall $Ni^{2+}$ concentration. After enduring 200 cycles within a voltage window of 2.6 to 4.3 V at a 1 C rate, the Ni ions in the LPO-Mo-NMCA do not undergo significant reduction into cubic phases (e.g., rock-salt or spinel-like phases), as evidenced by the averaged XAS spectrum in Fig. 8g-h. However, while this finding points to minimal large-scale formation of such byproducts, XAS alone cannot entirely exclude localized or minor structural changes after prolonged cycling, which will be further discussed alongside the electrochemical results. Owing to the resolution limitation of STXM, which is around a few tens of nanometers and predominantly determined by the quality of the focusing optics, [41] ptychography, offering an order of magnitude better spatial resolution, [42] was adopted to gain deeper morphological and chemical insights at the primary particle level.

The optical density maps at 852.7 and 855.1 eV, the energies at which the $Ni^{2+}$ and $Ni^{3+}$ spectrum exhibit maximum intensity, respectively (see the reference spectra in Fig. S12), reveal detailed morphological information, although they also contain some degree of chemical contrast (Fig. 9 and S15). At first glance, the size of the primary particles differs significantly between LPO-Mo-NMCA and NMCA. The grain boundaries often serve as quicker channels for Li diffusion, usually displaying a diffusivity three to ten times higher than in the bulk region. [43] As discussed earlier, in addition to the hollow space in the secondary NMCA particles, the smaller primary particle size results in a shorter diffusion length, potentially leading to improved electrochemical performance in terms of capacity and rate. In addition, the increased diffusion rate leads to a more even Li concentration across the secondary particle, mitigating the risk of intergranular fracture due to concentration inhomogeneity. [44-46] However, the overall electrochemical performance of NMCA is inferior to that of LPO-Mo-NMCA, as shown in Fig. 4. This is primarily due to imperfections in crystallinity, represented by the presence of $Ni^{2+}$, which generally lead to sluggish Li-ion (de)intercalation. [46] The qualitative chemical maps, derived from the optical density difference between 852.7 and 855.1 eV, also emphasize the presence of a $Ni^{2+}$-rich phase in both samples. The Mo dopant and LPO coating localize the distribution of $Ni^{2+}$ near the primary particle surface, where it forms as a byproduct during the synthesis process, whereas NMCA exhibits a widely spread $Ni^{2+}$-rich phase throughout both the secondary and primary particles. This structural integrity suggests that the LPO-Mo coating effectively alleviates interparticle strain, thereby preventing microcrack propagation and enhancing overall cycling stability. These findings underscore the LPO-Mo coating's role as a critical factor in improving the long-term durability of cathode materials under high-stress cycling conditions.

To elucidate the practical utility of the optimized LPO-Mo-NMCA (LPO-Mo-NMCA) cathode for advanced lithium-ion batteries (LIBs), pouch-type full cells integrating a pre-lithiated graphite anode and LPO-Mo-NMCA cathode were systematically fabricated, as schematically depicted in Fig. 10a. Pre-lithiation of the graphite anode was performed via direct contact with a lithium metal plate saturated in an electrolyte solution for 2 hours, [47] ensuring uniform lithiation. The capacity alignment between the LPO-Mo-NMCA cathode and graphite anode is presented in Fig. S16a. Notably, full cells with varying negative-to-positive (N:P) capacity ratios of 1.5:1, 1.8:1, and 2.0:1 exhibited initial discharge capacity of 166.63, 218.5, and 196.34 mA h $g^{-1}$ at 0.1 C, respectively (Fig. 10b**)**. The configuration optimized at an N:P ratio of 1.8:1 demonstrated superior electrochemical performance, delivering a discharge capacity of 218.5 mA h $g^{-1}$ with a capacity retention of 85 % over 110 cycles at a 0.1 C rate. The electrochemical reactions governing the charge and discharge processes in the full-cell configuration are as follows:

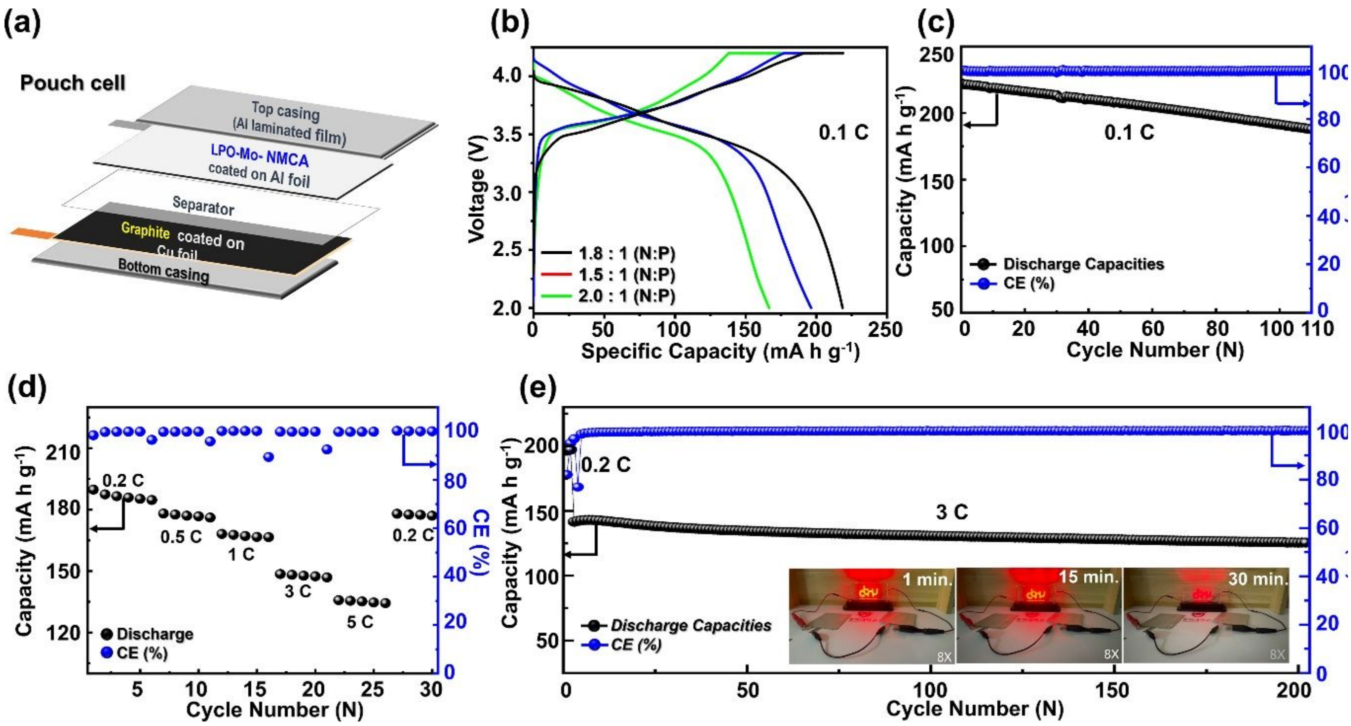


**Fig. 10** Performance evaluation of a pouch-type full-cell Li-ion battery: (a) Schematic illustration of the fabricated full-cell configuration; (b) initial charge-discharge profiles of electrodes with varying N:P mass ratios at a 0.1 C rate; (c) cyclic stability at 0.1 C for 110 cycles; (d)High-rate performance at different C rates; and (e) long-term cyclic stability at 3 C over 200 cycles for the optimal N:P ratio of 1.8:1 (inset: 8 V LED glowing for 30 minutes, demonstrating device functionality).

*Charge (Li-ion Extraction):*

*Cathode:* $LiNi_{0.9}Mn_{0.07}Co_{0.02}Al_{0.01}O_2 \rightarrow Li{-}xMn_{0.07}Co_{0.02}Al_{0.01} + xLi^+ + xe^-$ (1)

*Anode:* $C + xLi^+ + xe^- \rightarrow LixC_6$ (2)

*Discharge (Li-ion Insertion):*

*Cathode:* $Li_{1-x}Ni_{0.9}Mn_{0.07}Co_{0.02}Al_{0.01}O_2 + xLi^+ + xe^- \rightarrow Li\ Ni_{0.9}Mn_{0.07}Co_{0.02}Al_{0.01}O_2$ (3)

*Anode:* $LixC_6 \rightarrow C + xLi^+ + xe^-$ (4)

*Overall Reaction:*

$LiNi_{0.9}Mn_{0.07}Co_{0.02}Al_{0.02}O_2 + xC \leftrightarrow Li_{1-x}Ni_{0.9}Mn_{0.07}Co_{0.02}Al_{0.01}O_2 + LixC_6.$ (5)

As depicted in Fig. 10c and S16b, LPO-Mo-NMCA with graphite full-cell with an N:P ratio of 1.8:1 achieves a notable capacity retention of 85% after 110 cycles. This improvement is attributed to minimized electrode polarization, which enhances cyclability by reducing internal thermal energy dissipation during redox processes (Fig. S17a). Consequently, the cell maintains high energy efficiency, ensuring sustained performance over extended cycling. Further evaluate the high-rate capability of the LPO-Mo-NMCA with graphite full-cell configuration, the discharge capacities were assessed across a range of current rates from 0.2 to 5 C, as illustrated in Fig. 10d, with the corresponding charge-discharge profiles presented in Fig. S17b. At a 0.2 C rate, the full cell delivered a discharge capacity of 189.7 mA h $g^{-1}$, which decreased to 135.4 mA h $g^{-1}$ at 5 C, representing a retention of 71.3 %. Upon reverting to 0.2 C, the cell regained a capacity of 177.9 mA h $g^{-1}$, with a marginal capacity decay of 6.3 % and an average coulombic efficiency (CE) of ~97 % over the cycles. The cyclic performance, as shown in Fig. 10e, demonstrated robust stability at a 3 C rate. Remarkably, the optimized cell configuration with an N:P ratio of 1.8:1 retained ~89 % of its initial capacity after 200 cycles, outperforming cells with N:P ratios of 1.5:1 and 2.0:1 (Fig. S18), which exhibited retention values of 80 and 83%, respectively. These findings underscore the significance of the optimized mass ratio in achieving superior electrochemical performance. Moreover, the calculated energy density (E) for the optimized full cell reached ~369.23 Wh $kg^{-1}$, determined using the equation:[48]

$$E = c \times v/m \quad (6)$$

where C is the discharge capacity, V is the median voltage, and m represents the combined mass of the cathode and anode materials. Comparative analysis of Ni-rich cathode materials in full-cell lithium-ion batteries, detailing specific capacity, energy density, working voltage, with a direct comparison to the performance of our LPO-Mo-NMCA-based cell. The data showcases the advancements in energy density relative to previously reported values (Table S4), and highlights the practical energy density of ~369.2 Wh $kg^{-1}$, accounting for contributions from current collectors, aluminium plastic film, and electrolyte with a penalty factor of 30%. The high-performance of the LPO-Mo-NMCA pouch cell, featuring an ultra-compact design (16.4 $cm^2$ area and <1 mm thickness), was demonstrated through its ability to power an 8 V LED for over 30 minutes, as illustrated in Fig. 10e (inset). This demonstration underscores the potential of LPO-Mo-NMCA to enhance the cruising range of commercial EVs, emphasizing its promise as a high-performance cathode material for next-generation lithium-ion batteries. These findings reinforce its pivotal role in advancing renewable energy integration with sustainable transportation solutions.

 

## 4. Conclusions

The Mo-doped, $Li_3PO_4$-coated NMCA cathode represents a significant advancement in high-energy-density lithium-ion batteries, demonstrating superior structural stability and electrochemical performance. Mo doping effectively stabilizes the internal structure, reducing the propensity for cation migration and enhancing the robustness of the lattice framework. Meanwhile, the $Li_3PO_4$ coating acts as a protective barrier, suppressing side reactions and enhancing interfacial stability, which collectively improve lithium-ion transport and mitigate capacity fade. Electrochemical performance evaluations demonstrate that the LPO-Mo-NMCA cathode achieves excellent capacity retention of 87% after 200 cycles at 1 C and 91 % at 3 C, outperforming its unmodified counterparts. Furthermore, microstructural analyses confirm the mitigation of microcrack propagation and surface degradation, reinforcing the cathode's durability under high-stress cycling conditions. The synergy between Mo doping and LPO coating provides a compelling strategy for addressing the challenges associated with nickel-rich cathodes, offering a pathway to improved performance and reliability. Additionally, pouch-type full cells incorporating LP-Mo-NMCA and a graphite anode demonstrate an initial discharge capacity of 218 mA h $g^{-1}$ at 0.1 C, achieving 85 % capacity retention after 110 cycles, and maintaining 89% retention at 3C over 200 cycles within the voltage range of 2.0 to 4.2 V. Importantly, these full cells deliver a practical energy density of 369.2 Wh $kg^{-1}$ at 0.1C. These findings underscore LPO-Mo-NMCA as a promising cathode material for next-generation lithium-ion batteries, bridging the critical balance between high energy density and long-term cycling stability.

## Acknowledgements

This work was supported by the National Research Foundation of Korea (NRF) and the Commercialization Promotion Agency for R&D Outcomes (COMPA) funded by the Ministry of Science and ICT (Grant No.: RS-2023-00217581, RS-2023-00304768). This research used resources of the Advanced Light Source, which is a DOE Office of Science User Facility under contract no. DE-AC02-05CH11231.

## Notes and references

1. Q. Huang, Z. Hu, Z. Dai, X. Lv, X. Zhang, E. Fan, R. Chen, F. Wu and L. Li, *Energy Storage Mater.*, 2024, **72**, 103695.
2. X.-H. Meng, D. Xiao, Z.-Y. Zhou, W.-Z. Liu, J.-L. Shi, L.-J. Wan and Y.-G. Guo, *J. Am. Chem. Soc.*, 2024 **146**, 14889-14897.
3. Y. Sun, W. Huang, G. Zhao, Q. Liu, L. Duan, S. Wang, Q. An, H. Wang, Y. Yang and C. Zhang, *ACS Energy Lett.*, 2023, **8**, 1629-1638.
4. J. Zhu, Y. Li, L. Xue, Y. Chen, T. Lei, S. Deng and G. Cao, *J. Alloys Compd.*, 2019, **773**, 112-120.
5. N.-Y. Park, G.-T. Park, S.-B. Kim, W. Jung, B.-C. Park and Y.-K. Sun, *ACS Energy Lett.*, 2022, **7**, 2362-2369.
6. P. Ju, L. Ben, Y. Li, H. Yu, W. Zhao, Y. Chen, Y. Zhu and X. Huang, *ACS Energy Lett.*, 2023, **8**, 3800-3810.
7. H. H. Ryu, N. Y. Park, D. R. Yoon, U. H. Kim, C. S. Yoon and Y. K. Sun, *Adv. Energy Mater.*, 2020, **10**, 2000495.
8. J.-H. Kim, K.-J. Park, S. J. Kim, C. S. Yoon and Y.-K. Sun, *J. Mater. Chem. A*, 2019, **7**, 2694-2701.
9. X. Zhang, E. Fan, J. Lin, Y. Zhao, Q. Huang, S. Ma, R. Chen, F. Wu and L. Li, *Energy Storage Mater.*, 2025, **74**, 103914.
10. G.-T. Park, H.-H. Ryu, N.-Y. Park, C. S. Yoon and Y.-K. Sun, *J. Power Sources*, 2019, **442**, 227242.
11. Y. Sun, Z. Liu, X. Chen, X. Yang, F. Xiang and W. Lu, *Electrochim. Acta*, 2021, **376**, 138038.
12. H. Zhang, L. Qin, X. Huang, Y. Fang, H. Yu, Q. Cheng and H. Jiang, *J. Mater. Chem. A*, 2024, **12**, 24542-24548.
13. S. Wang, M. Zhang, Y. Yan, D. Zhang, Y. Wang, G. Cao, J. Shi and X. Sun, *J. Mater. Chem. A*, 2024, **12**, 33689-33698.
14. G.-T. Park, D. R. Yoon, U.-H. Kim, B. Namkoong, J. Lee, M. M. Wang, A. C. Lee, X. W. Gu, W. C. Chueh and C. S. Yoon, *Energy Environ. Sci.*, 2021, **14**, 6616-6626.
15. H. H. Sun, U.-H. Kim, J.-H. Park, S.-W. Park, D.-H. Seo, A. Heller, C. B. Mullins, C. S. Yoon and Y.-K. Sun, *Nat. Commun.*, 2021, **12**, 6552.
16. T. Yang, K. Zhang, Y. Zuo, J. Song, Y. Yang, C. Gao, T. Chen, H. Wang, W. Xiao and Z. Jiang, *Nat. Sustain.*, 2024, **7**, 1204-1214.
17. U.-H. Kim, G.-T. Park, B.-K. Son, G. W. Nam, J. Liu, L.-Y. Kuo, P. Kaghazchi, C. S. Yoon and Y.-K. Sun, *Nat. Energy*, 2020, **5**, 860-869.
18. M. Xu, B. Sheng, Y. Cheng, J. Lu, M. Chen, P. Wang, B. Liu, J. Chen, X. Han and M.-S. Wang, *Nano Res.*, 2024, **17**, 4192-4202.
19. D. Becker, M. Börner, R. Nölle, M. Diehl, S. Klein, U. Rodehorst, R. Schmuch, M. Winter and T. Placke, ACS Appl. Mater. Interfaces, 2019 **11**, 18404-18414.
20. F. Reissig, J. Ramirez-Rico, T. J. Placke, M. Winter, R. Schmuch and A. Gomez-Martin, *Batteries*, 2023, **9**, 245.
21. T. J. Embleton, J. Yun, J. H. Choi, J. Kim, S. Choi, C. Lee, Y. Son and P. Oh, *Small*, 2023, **19**, 2206576.
22. M. Qi, L. Wang, X. Huang, M. Ma and X. He, *Small*, 2024, 2402443.
23. X. He, J. Shen, B. Zhang, Z. Xiao, L. Ye, Q. Mao, Q. Zhong and X. Ou, *Adv. Funct. Mater.*, 2024, **34**, 2401300.
24. J. H. Choi, T. J. Embleton, K. Ko, H. Jang, Y. Son, J. Park, S. Lee and P. Oh, *ChemElectroChem*, 2024, **11**, e202300705.
25. S. Mitra and C. Sudakar, *Battery Energy*, 2024, **3**, 20230066.
26. S. Li, J. Wu, J. Li, G. Liu, Y. Cui and H. Liu, *ACS Appl. Energy Mater.*, 2021, **4**, 2257-2265.
27. X. Qu, Z. Yu, D. Ruan, A. Dou, M. Su, Y. Zhou, Y. Liu and D. Chu, *ACS Sus. Chem. Eng.*, 2020, **8**, 5819-5830.
28. Y. Shao, J. Xu, A. Amardeep, Y. Xia, X. Meng, J. Liu and S. Liao, *Small Methods*, 2024, 2400256.
29. S. Deng, X. Li, Z. Ren, W. Li, J. Luo, J. Liang, J. Liang, M. N. Banis, M. Li and Y. Zhao, *Energy Storage Mater.*, 2020, **27**, 117-123.
30. T. Fu, D. Lu, Z. Yao, Y. Li, C. Luo, T. Yang, S. Liu, Y. Chen, Q. Guo and C. Zheng, *J. Mater. Chem. A*, 2023, **11**, 13889-13915.
31. Q. Gan, N. Qin, Z. Wang, Z. Li, Y. Zhu, Y. Li, S. Gu, H. Yuan, W. Luo and L. Lu, *ACS Appl. Energy Mater.*, 2020, **3**, 7445-7455.
32. P. Zou, Z. Lin, M. Fan, F. Wang, Y. Liu and X. Xiong, *Appl. Surf. Sci.*, 2020, **504**, 144506.
33. L. Wang, Y. Chu, Y. Nong, F. Zheng, Y. Li, Y. Huang, Y. Li, Q. Pan, H. Wang and Q. Li, *ACS Sus. Chem. Eng.*, 2022, **10**, 7883-7895.

 

34. P. Dai, X. Kong, H. Yang, J. Li, J. Zeng and J. Zhao, *ACS Sus. Chem. Eng*, 2022, **10**, 4381-4390.
35. D. Y. Hwang, C. Y. Kang, J. R. Yoon and S. H. Lee, *Int. J. Energy Res.,* 2022, **46**, 15244-15253.
36. T. Fu, Y. Li, Z. Yao, T. Guo, S. Liu, Z. Chen, C. Zheng and W. Sun, *Small*, 2024, **20**, 2402339.
37. F. A. Susai, A. Bano, S. Maiti, J. Grinblat, A. Chakraborty, H. Sclar, T. Kravchuk, A. Kondrakov, M. Tkachev and M. Talianker, *J. Mater. Chem. A*, 2023, **11**, 12958-12972.
38. H.-H. Ryu, H.-W. Lim, S. G. Lee and Y.-K. Sun, *Energy Storage Mater.*, 2023, **59**, 102771.
39. R. Lin, S.-M. Bak, Y. Shin, R. Zhang, C. Wang, K. Kisslinger, M. Ge, X. Huang, Z. Shadike and A. Pattammattel, *Nat. Commu.*, 2021, **12**, 2350.
40. R. J. Clément, Z. Lun and G. Ceder, *Energy Environ. Sci.*, 2020, **13**, 345-373.
41. W. Chao, B. D. Harteneck, J. A. Liddle, E. H. Anderson and D. T. Attwood, *Nature*, 2005, **435**, 1210-1213.
42. D. A. Shapiro, Y.-S. Yu, T. Tyliszczak, J. Cabana, R. Celestre, W. Chao, K. Kaznatcheev, A. L. D. Kilcoyne, F. Maia and S. Marchesini, *Nature Photonics*, 2014, **8**, 765-769.
43. S. Yang, B. Yan, L. Lu and K. Zeng, *RSC Adv.*, 2016, **6**, 94000-94009.
44. T. Sattar, S.-H. Lee, B.-S. Jin and H.-S. Kim, *Sci. Rep.*, 2020, **10**, 8562.
45. H.-H. Ryu, B. Namkoong, J.-H. Kim, I. Belharouak, C. S. Yoon and Y.-K. Sun, *ACS Energy Lett.*, 2021, **6**, 2726-2734.
46. J. Min, L. M. Gubow, R. J. Hargrave, J. B. Siegel and Y. Li, *Energy Environ. Sci.*, 2023, **16**, 3847-3859.
47. Z. Zhao, Z. Wang, D. K. Denis, X. Sun, J. Zhang, L. Hou, X. Zhang and C. Yuan, *Electrochim. Acta*, 2019, **307**, 20-29.
48. W. Zhang, L. Liang, F. Zhao, Y. Liu, L. Hou and C. Yuan, *Electrochim. acta*, 2020, **340**, 135871.

 

**Data Availability Statement**

The authors confirm that the data supporting the findings of this study are available within the article [and/or its ESI†].